

An *XMM-Newton* observation of the Lagoon Nebula and the very young open cluster NGC 6530*

G. Rauw^{1**}, Y. Nazé^{1***}, E. Gosset^{1**}, I.R. Stevens², R. Blomme³, M.F. Corcoran⁴, J.M. Pittard⁵, and M.C. Runacres³

¹ Institut d'Astrophysique, Université de Liège, Allée du 6 Août, Bât B5c, B-4000 Liège (Sart Tilman), Belgium

² School of Physics & Astronomy, University of Birmingham, Edgbaston Birmingham B15 2TT, UK

³ Royal Observatory of Belgium, Avenue Circulaire 3, B-1180 Brussels, Belgium

⁴ USRA/HEASARC Goddard Space Flight Center, Greenbelt, MD 20771, USA

⁵ Department of Physics & Astronomy, University of Leeds, Leeds LS2 9JT, UK

Received date / Accepted date

Abstract. We report the results of an *XMM-Newton* observation of the Lagoon Nebula (M8). Our EPIC images of this region reveal a cluster of point sources, most of which have optical counterparts inside the very young open cluster NGC 6530. The bulk of these X-ray sources are probably associated with low and intermediate mass pre-main sequence stars. One of the sources experienced a flare-like increase of its X-ray flux making it the second brightest source in M8 after the O4 star 9 Sgr. The X-ray spectra of most of the brightest sources can be fitted with thermal plasma models with temperatures of $kT \sim$ a few keV. Only a few of the X-ray selected PMS candidates are known to display $H\alpha$ emission and were previously classified as classical T Tauri stars. This suggests that most of the X-ray emitting PMS stars in NGC 6530 are weak-line T Tauri stars. In addition to 9 Sgr, our EPIC field of view contains also a few early-type stars. The X-ray emission from HD 164816 is found to be typical for an O9.5 III-IV star. At least one of the known Herbig Be stars in NGC 6530 (LkH α 115) exhibits a relatively strong X-ray emission, while most of the main sequence stars of spectral type B1 and later are not detected. We also detect (probably) diffuse X-ray emission from the Hourglass Region that might reveal a hot bubble blown by the stellar wind of Herschel 36, the ionizing star of the Hourglass Region.

Key words. ISM: individual objects: M8 – open clusters and associations: individual: NGC 6530 – Stars: early-type – Stars: pre-main sequence – X-rays: stars

1. Introduction

The Lagoon Nebula (M8 = NGC 6523) is one of the closest and brightest H II regions in the Galaxy. The nebula is ionized by the O4 V star 9 Sgr and the binary system HD 165052 (O6.5 V + O6.5 V). M8 harbours also the very young open cluster NGC 6530 as well as a compact H II region, the so-called Hourglass Region (hereafter HG), which is ionized by the O7 V star Herschel 36. NGC 6530 is believed to be at the origin of a sequential star formation process inside the Lagoon Nebula (Lightfoot et al. 1984). NGC 6530 most probably formed from a pre-existing massive molecular cloud. The ionizing radiation of the newly formed hot stars in the cluster then created a cavity allowing us to see inside the parent molecular cloud. Furthermore, NGC 6530 may have triggered the formation of 9 Sgr, which subsequently

caused the formation of the massive protostar Herschel 36 (= HD 164740, hereafter H 36).

According to van den Ancker et al. (1997), star formation within NGC 6530 started a few 10^7 years ago and is probably still ongoing. Sung et al. (2000) found that 9 Sgr and H 36 are well fitted to an isochrone of age ~ 1.5 Myr, while the age of the stars at the fainter end of the populated part of the main-sequence of NGC 6530 is about 4 Myr and the massive pre-main sequence star LkH α 112 should be only about 0.4 Myr old. Using *UBVRI* and $H\alpha$ photometry of NGC 6530, Sung et al. (2000) identified 58 pre-main sequence (PMS) stars with $H\alpha$ emission as well as 17 PMS candidates (PMSc).

Many recent studies of the Lagoon Nebula focused on the Hourglass Region as seen in different wavebands. The HG nebula is believed to be an ionized cavity in an inhomogeneous clumpy molecular cloud. The apparent bipolar structure in the optical band most likely results from a non-uniform extinction along the line of sight. Woodward et al. (1986) proposed a

* Based on observations with *XMM-Newton*, an ESA Science Mission with instruments and contributions directly funded by ESA Member states and the USA (NASA).

** Research Associate FNRS (Belgium)

*** Research Fellow FNRS (Belgium)

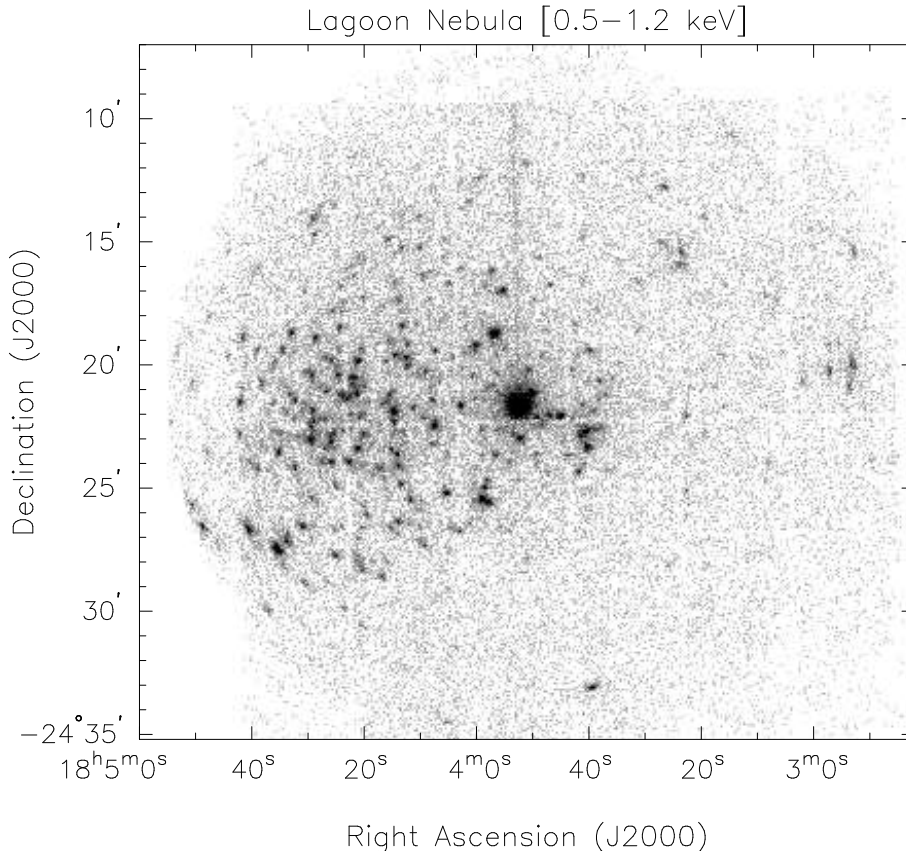


Fig. 1. Combined EPIC-MOS1, -MOS2 and -pn image of the field of view around 9 Sgr. To avoid contamination by the hard straylight photons from GX 9+1, we restricted the image extraction to events in the soft energy band 0.5 – 1.2 keV only. The bright source in the center is 9 Sgr. Note that the roughly vertical trail above 9 Sgr is due to events from 9 Sgr that arrived during the readout of the pn detector.

model in which two high-density knots on the eastern side protect the material behind them from the ionizing radiation while the western edge of the HG would be defined by a foreground cloud obscuring H 36.

In the present paper, we discuss an *XMM-Newton* observation of M 8, that reveals a number of point sources towards the open cluster NGC 6530. In Sects. 2 and 3, we investigate the light curves and spectra of the brightest sources and we discuss their possible association with PMS stars in NGC 6530. In Section 4, we discuss also the soft X-ray emission from the HG nebula. Finally, our conclusions are presented in Section 5.

2. X-ray sources inside the Lagoon Nebula

The Lagoon Nebula was observed serendipitously for about 20 ksec with the *XMM-Newton* observatory (Jansen et al. 2001) during our AO1 observation of the O4 V star 9 Sgr (JD 2451976.978 – 2451977.239). The two EPIC-MOS instruments were operated in the full frame mode (Turner et al. 2001) whilst the EPIC-pn camera was used in the extended full frame mode (Strüder et al. 2001). All three EPIC instruments used the thick filter to reject optical light. We used version 5.1 of the *XMM-Newton* Science Analysis System (SAS) to reduce the raw EPIC data. More details on the pipeline processing of the data are given in the paper dealing with the 9 Sgr data (Rauw

et al. 2002).

The combined EPIC soft band (0.5 – 1.2 keV) X-ray image around 9 Sgr reveals a number of point-like (and maybe also diffuse) sources (see Fig. 1). Figure 2 displays the EPIC contours of the X-ray sources superimposed on a Digital Sky Survey image of M 8. This image indicates that most of the fainter sources are located in the region of the very young open cluster NGC 6530. One rather bright and apparently diffuse source (to the south-west of 9 Sgr) is associated with the Hourglass Region.

Because of the contamination of the EPIC data by hard straylight photons from the nearby LMXB GX 9+1, the source detection was performed on the soft band images (i.e. where there is no contamination) only. For details on the properties of the straylight, we refer again to the work of Rauw et al. (2002). Using the SAS source detection algorithms (see e.g. Hasinger et al. 2001), we find 250 sources that are detected simultaneously in the MOS1, MOS2 and pn images with a combined logarithmic likelihood

$$\sum_{i=1}^3 -\ln p_i \geq 9.0$$

where the summation runs over the MOS1, MOS2 and pn images. In this formula, p_i stands for the probability that a

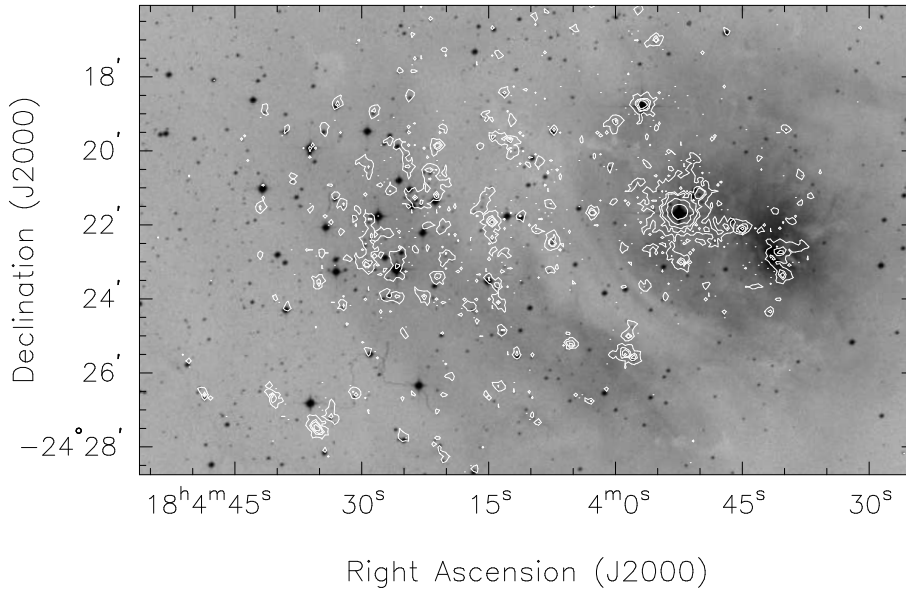


Fig. 2. EPIC X-ray contours (corresponding to the combined MOS1 + MOS2 + pn data in the 0.5 – 1.2 keV range) superimposed on a DSS optical image of the Lagoon Nebula. The different contours correspond to 5, 15, 24, 50 and 200 counts in the X-ray image.

random Poissonian fluctuation may have caused the observed source counts in the image of the detector i . We then inspected each source manually to reject spurious detections due e.g. to hot pixels. This resulted in a total of 220 confirmed detections. Out of these 220 sources, 117 have a combined likelihood ≥ 20.0 and are detected in the individual images from all three EPIC instruments with $-\ln p_i \geq 3.0$. With these criteria, the probability of detecting a spurious source within a $15'' \times 15''$ detection element should be $\sim 2 \times 10^{-9}$ and we therefore expect much less than one spurious detection over the entire EPIC field of view. To this list we add two sources that are not detected in at least one of the instruments because they fall outside its field of view, but are clearly detected in the remaining instruments. This gives us a total of 119 highly significant detections. In the following, we will restrict our discussion to these latter objects (see Fig. 3). The faintest sources in this category have about 10^{-3} cts s^{-1} over the 0.5 – 1.2 keV band of the MOS instruments. Assuming a 1 keV thermal spectrum with a neutral hydrogen column density of 0.17×10^{22} cm^{-2} (see also Sect. 3 below), the faintest sources correspond to an observed flux of about 8.9×10^{-15} $erg\ cm^{-2}\ s^{-1}$ and an unabsorbed flux of 13.1×10^{-15} $erg\ cm^{-2}\ s^{-1}$ in the 0.5 – 5.0 keV energy range. Note that the corresponding observed flux in the 0.5 – 1.2 keV soft band would be 5.2×10^{-15} $erg\ cm^{-2}\ s^{-1}$.

The most complete compilation of optical sources in NGC 6530 is the catalogue provided by Sung et al. (2000). These authors present *UBVRI* and $H\alpha$ photometry of 887 stars brighter than $V = 17$ and spread over an area from RA = 18:03:20 to 18:04:52 and from DEC = $-24:11:45$ to $-24:32:20$ (Equinox J2000.0). They include also a deeper *HST* WFPC2 observation of the Hourglass Region in their analysis.

We find that a total of 111 out of 119 X-ray sources detected with *XMM* fall inside the area covered by Sung et al. (2000).

We have cross-correlated the positions of these sources with the Sung et al. catalogue. In order to determine the optimal radius of cross-correlation, we adopted the approach outlined by Jeffries et al. (1997). We generated the cumulative distribution of the number of detected sources as a function of the cross-correlation radius r (see Fig. 4) and modelled this distribution assuming that it can be represented by means of an expression taken from Jeffries et al.:

$$\Phi(d \leq r) = A \left[1 - \exp\left(\frac{-r^2}{2\sigma^2}\right) \right] + (N - A) [1 - \exp(-\pi B r^2)]$$

Here N , A , σ and B stand for the total number of cross-correlated X-ray sources ($N = 111$), the number of true correlations, the uncertainty on the X-ray source position and the surface density of optical sources respectively. The first term in this expression stands for the cumulative distribution of true correlations whereas the second term yields the cumulative number of spurious correlations. A , σ and B are fitting parameters and were obtained from the best fit to the distribution displayed in Fig. 4. We obtain $A = 87.0$, $\sigma = 2.9$ arcsec and $B = 4.7 \times 10^{-4}$ $arcsec^{-2}$. The optimal correlation radius, i.e. the radius that includes the bulk of the true correlations while simultaneously limiting contamination by spurious correlations, is found to be around 9 arcsec. For $r = 9$ arcsec, we expect to achieve 86 true and only 3 spurious correlations.

There are two limitations to this procedure. Strictly speaking, the above expression for the spurious detections is down-right valid for a uniform distribution of the optical sources over the investigated area. Though this is not the case for the optically brightest objects, Fig. 1 of Sung et al. (2000) indicates that this should be a fairly good approximation for the fainter stars. Another issue is that we assume that a single correlation radius can be used over the entire field of view. A radius of 9 arcsec corresponds roughly to 1.5 times the in-orbit FWHM of the on-axis point spread function (PSF) of the *XMM* mirror

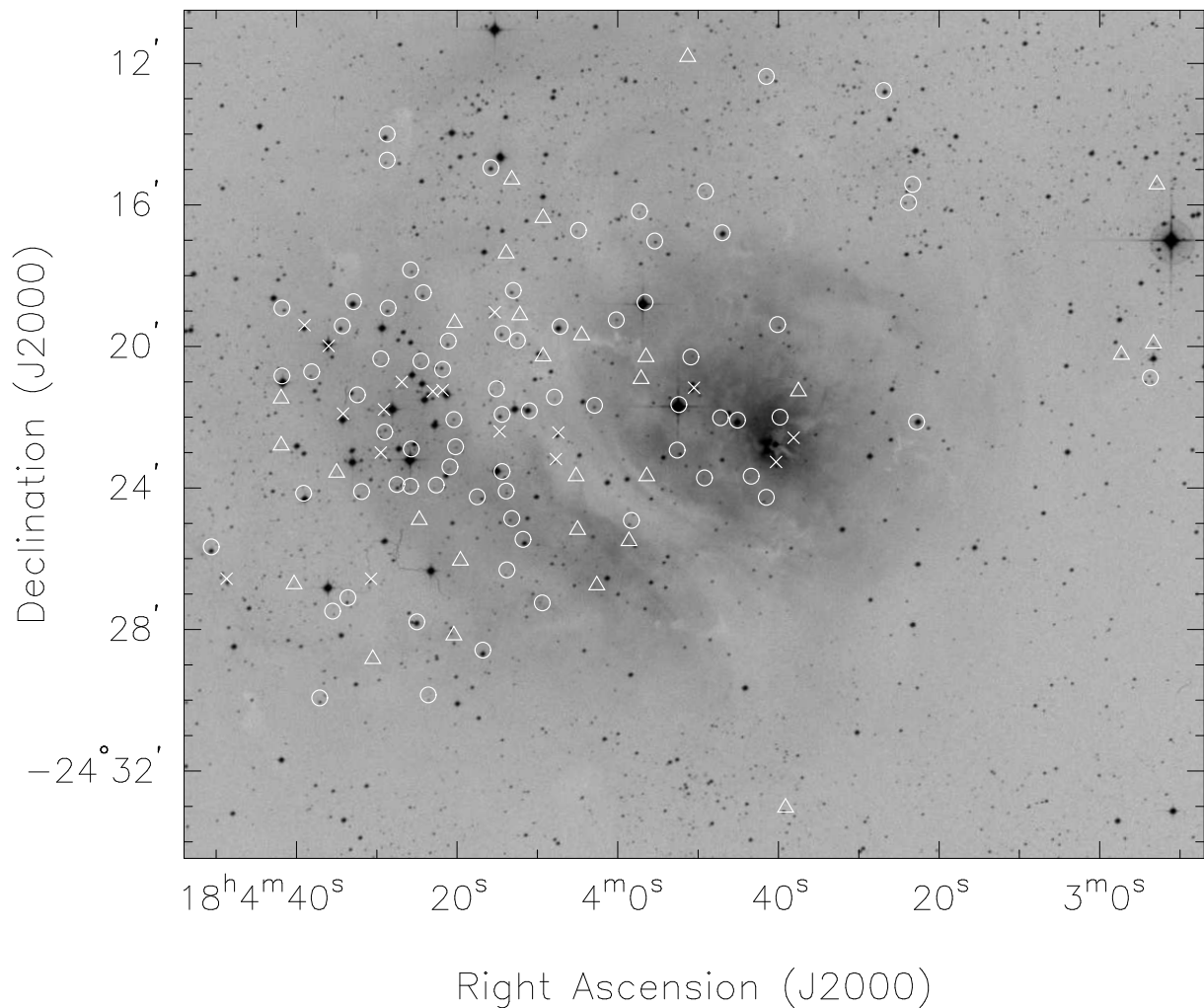


Fig. 3. DSS optical image of the Lagoon Nebula complex together with the positions of the highly significant sources. Open circles and crosses stand for X-ray sources having respectively a single or several counterparts in the Sung et al. (2000) catalogue. The open triangles indicate the positions of sources with no counterpart in the latter catalogue (nor in the SIMBAD database).

modules at 1.5 keV (Jansen et al. 2001). At large off-axis angles, the quality of the PSF progressively degrades and the half energy width increases by nearly a factor of two (Stockman et al. 1998). Our optimal radius should therefore be seen as some sort of weighted average for different off-axis angles.

Within a correlation radius of 9 arcsec, we find that:

- the brightest X-ray source is associated with the O4 V((f⁺)) star 9 Sgr. The data on this star have been analysed elsewhere (Rauw et al. 2002) and we will not repeat this discussion here.
- a probably diffuse X-ray source is associated with the Hourglass Region. We shall return to the HG in Sect. 4.
- 72 X-ray sources have a single optical counterpart within a radius of less than 9 arcsec. The average angular separation between the X-ray source and the optical counterpart is (4.1 ± 2.1) arcsec. The brightest soft X-ray sources in this category are HD 164816 (O9.5 III-IV) and SCB 731. The latter is a very red 16th magnitude star without outstanding features (such as H α emission) in its optical photometry.

The X-ray source associated with SCB 731 appears elongated since it lies rather far off-axis.

- 17 X-ray sources have two or more optical stars falling within the 9 arcsec radius. Seven of these sources have at least one known H α emission star inside their ‘error box’.
- 28 sources do not have an optical counterpart in the catalogue of Sung et al. We have cross-correlated these sources with the Guide Star Catalogue (GSC¹). In most cases, we find one or several GSC objects inside the 9 arcsec radius. These optical counterparts are usually very faint (V or $R \geq 17$) except for sources #91, 92 and 94 that have counterparts with R magnitudes 15.0, 14.6 and 13.3 respectively (note that these sources fall outside the area investigated by Sung et al.). Sources #93, 96, 98, 99, 100, 101, 102 and 112 have no GSC counterpart. Most of the objects in Table 3 are therefore X-ray sources with high

¹ The Guide Star Catalogue-II is a joint project of the Space Telescope Science Institute and the Osservatorio Astronomico di Torino.

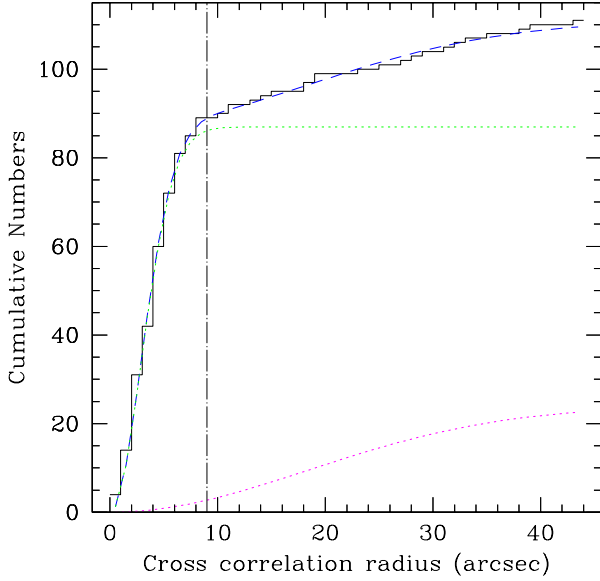


Fig. 4. Cumulative numbers of correlations between the X-ray detections and the Sung et al. (2000) catalogue as a function of correlation radius. The dotted curves correspond to the best fitting expressions for the real and spurious correlations. The dashed curve yields the sum of these terms and the dash-dotted vertical line corresponds to the optimal correlation radius of 9 arcsec.

L_X/L_{vis} ratios. Given the galactic coordinates of NGC 6530 ($l_{\text{II}} = 6.14^\circ$, $b_{\text{II}} = -1.38^\circ$), the total galactic column density along our line of sight in this direction must be extremely large and the number of extragalactic sources in our soft detection energy band should be extremely low.

The sources of the last three categories are listed in Tables 1, 2 and 3 respectively. Along with our own source numbering, we list the source designation following the naming conventions recommended by the *XMM* SOC and the IAU (see the *XMM-Newton* Newsletter #4, April 2001): the XMMUJ prefix is followed by the right ascension HHMMSS.s (in hours, minutes, seconds and tenths of seconds) and the declination of the source \pm DDMMSS (in degrees, arcminutes and arcseconds). Note that the coordinates refer to equinox J2000 and are truncated, not rounded.

2.1. Light curves

We have extracted light curves and spectra for the brightest objects. Except for sources near the edge of the field of view, we used a circular extraction region with a radius between 19 and 40 arcsec depending on the angular separation between neighbouring X-ray sources. For sources near the edge of the field of view, we used elliptical extraction regions to match as closely as possible the shape of the point spread function. The light curves and spectra were accumulated over the PI range 200 to 10000 (corresponding roughly to $E \in [0.2, 10.0]$ keV), except for objects that are contaminated by the straylight. In the latter cases, we extracted light curves only (i.e. no spectra) over the PI range 200 to 1500 (i.e. $E \in [0.2, 1.5]$ keV).

For all the light curves we adopted time bins of 400 s. The light curves were tested for variability using a Kolmogorov-Smirnov test against a model of constant count rate. Among the sources with a single optical counterpart, SCB 731, the second brightest X-ray source, is clearly variable: the light curve (extracted over an elliptical region adapted to the shape of the PSF) reveals a strong X-ray flare towards the end of our observation (Fig. 5). The X-ray flux suddenly rises by nearly two orders of magnitude and after about 2000 s starts to decline again.

SCB 182 and source #99 show some marginal variability in their light curves. The behaviour is the same in all three EPIC instruments, but the variability occurs at a rather low level so that it is found not to be significant by the Kolmogorov-Smirnov test (at the $P > 95\%$ confidence level). A Fourier technique detects slow variability in the light curve of source #99 at the 99% confidence level.

None of the other relatively bright sources turned out to display significant variability (95% level) over the duration of our observation.

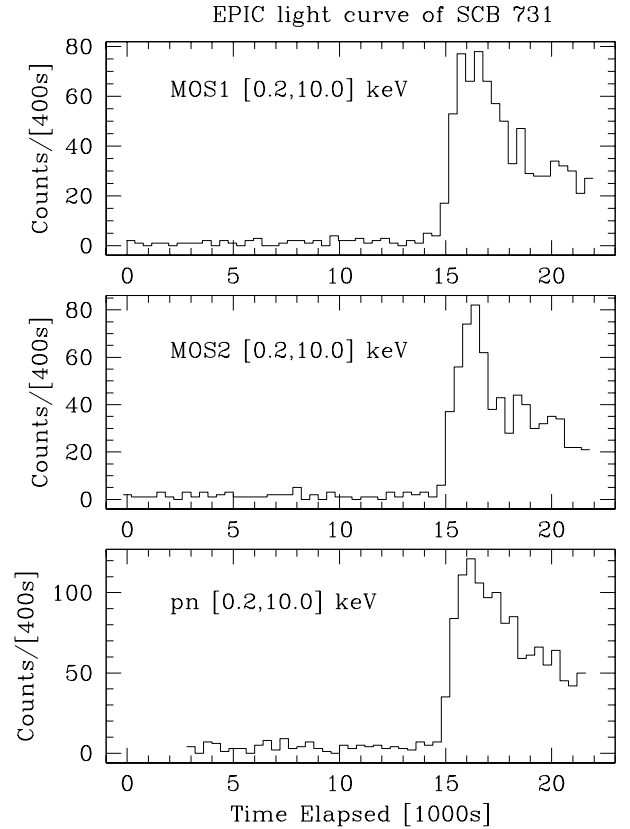


Fig. 5. EPIC light curves of the X-ray source #66 (XMMUJ180435.5–242729) associated with SCB 731. We have also extracted the light curve of a nearby background region (not shown here). The latter does not display any variability. The zero time in our light curves corresponds to JD 2451976.982.

Table 1. X-ray sources detected in NGC 6530 and found to have a single counterpart in the catalogue of Sung et al. (2000) or in the SIMBAD database. The first and second columns yield the number of the X-ray source as well as the name according to the conventions for serendipitous *XMM-Newton* sources. Columns [3], [4] and [5] provide the vignetting and background corrected EPIC-MOS and pn count rates in the 0.5 – 1.2 keV band. For sources affected by the gaps between the detectors, we do not quote the count rate for the corresponding instrument. The number of the optical counterpart from Sung et al. (2000) and the separation from the position of the X-ray source are given in columns [6] and [7]. The photometric data are taken from Sung et al. (2000), except for V 1752 Sgr. Column [11] indicates whether variability is detected at the 95% confidence level (Y) or not (N). Those sources flagged with a ‘?’ show some hints of variability in their light curve, but this is not found to be significant by the Kolmogorov-Smirnov test. Finally, the last column yields information about the spectral types, pre-main sequence classification and the membership probability (P_μ) according to the proper motion study of van Altena & Jones (1972).

Source #	XMMUJ	MOS1 10^{-3} cts s $^{-1}$	MOS2 10^{-3} cts s $^{-1}$	pn 10^{-3} cts s $^{-1}$	SCB	d (arcsec)	V	B – V	V – I	Variability	Comments
[1]	[2]	[3]	[4]	[5]	[6]	[7]	[8]	[9]	[10]	[11]	[12]
1	180253.7–242053	4.1 ± 1.0	2.8 ± 1.1	5.2 ± 1.6		8.4	15.80				V 1752 Sgr = PMS
2	180322.8–242208	3.0 ± 0.6	1.4 ± 0.4		7	3.9	10.62	0.96	1.07	N	
3	180323.3–241525	1.4 ± 0.7	1.5 ± 0.7	5.2 ± 1.0	20	7.0	15.17	1.28	1.53		
4	180323.8–241556	2.7 ± 0.6	3.1 ± 0.6	2.0 ± 0.8	28	5.7	15.51	1.25	1.52		
5	180326.9–241246	2.9 ± 0.7	2.1 ± 0.6	6.2 ± 1.2	47	1.4	11.83	0.26	0.45		$P_\mu = 0.80$
6	180339.8–242200	1.6 ± 0.4	1.7 ± 0.4	2.8 ± 0.7	1032	8.8	18.72		2.98		PMS
7	180340.1–241923	1.6 ± 0.4	1.7 ± 0.4	2.8 ± 0.7	138	3.5	15.05	1.24	1.41		
8	180341.5–241222	1.5 ± 0.5	1.0 ± 0.4	1.7 ± 0.7	151	0.8	15.38	1.33	1.58		
9	180341.5–242416	1.9 ± 0.4	2.2 ± 0.4	4.3 ± 0.7	157	5.7	15.44	1.47	1.93		PMS
10	180343.4–242340	2.6 ± 0.5	2.0 ± 0.4	3.8 ± 1.0	174	4.1	16.90	1.44	1.88		
11	180345.1–242205	5.1 ± 0.6	7.3 ± 0.7	11.5 ± 1.2	182	0.5	9.95	0.18	0.41	?	B2.5V, $P_\mu = 0.86$
12	180347.0–241647	0.8 ± 0.3	1.6 ± 0.4	1.6 ± 0.5	199	1.8	10.75	0.09	0.15		
13	180347.2–242201	1.0 ± 0.6	1.8 ± 0.7	3.8 ± 0.9	202	4.5	16.64	1.55	2.13		
14	180349.1–241537	0.7 ± 0.3	0.8 ± 0.3	1.7 ± 0.6	220	4.1	16.87	1.31	1.55		
15	180349.2–242343	0.8 ± 0.4	0.7 ± 0.3	2.4 ± 0.6	223	6.0	16.85	1.35	1.72		
16	180350.9–242018	2.5 ± 0.5	1.7 ± 0.4	3.6 ± 0.9	238	5.6	16.96	1.44	2.07		
17	180352.6–242256	4.3 ± 0.6	4.6 ± 0.6	8.7 ± 1.2	253	6.4	13.80	1.23	1.49	N	$P_\mu = 0.00$
18	180355.4–241701	2.8 ± 0.5	4.7 ± 0.6	7.0 ± 1.1	274	1.8	14.61	1.06	1.18	N	
19	180356.6–241845	14.3 ± 1.0	16.6 ± 1.1	35.8 ± 2.0	282	4.1	6.99	0.02	0.00	N	HD 164816 (O9.5 III-IV)
20	180357.3–241611	1.3 ± 0.4	1.3 ± 0.4	4.2 ± 0.8	285	1.2	16.27	1.20	1.41		
21	180358.3–242455	3.7 ± 0.5	3.4 ± 0.5	3.7 ± 0.9	295	5.6	15.51	1.40	1.84	N	
22	180400.2–241915	3.2 ± 0.5	4.0 ± 0.6	6.9 ± 1.0	314	3.4	15.28	1.14	1.36	N	
23	180402.9–242140	4.4 ± 0.6	5.4 ± 0.6	5.3 ± 0.9	340	0.1	14.85	1.35	1.59	N	
24	180404.9–241643	1.3 ± 0.4	0.7 ± 0.3	2.5 ± 0.6	360	4.3	16.31	1.40	1.64		
25	180407.2–241926	1.5 ± 0.5	1.3 ± 0.4	3.6 ± 0.7	379	2.7	10.76	0.25	0.48		$P_\mu = 0.00$
26	180407.9–242126	1.7 ± 0.4	2.0 ± 0.4	3.5 ± 0.8	387	0.6	16.43	1.32	1.68		
27	180409.4–242715	2.4 ± 0.5	2.1 ± 0.5	3.8 ± 0.8	410	6.2	16.69	1.60	1.86		
28	180411.0–242149	2.0 ± 0.4	1.6 ± 0.4	3.8 ± 0.8	426	4.7	10.37	0.12	0.23		B3Ve, $P_\mu = 0.84$
29	180411.8–242527	1.7 ± 0.4	2.6 ± 0.5	4.2 ± 0.9	432	4.1	11.69	0.24	0.44		A0, $P_\mu = 0.52$
30	180412.5–241950	4.0 ± 0.6	2.9 ± 0.5	11.1 ± 1.5	440	7.0	15.99	1.32	1.70	N	PMS
31	180413.0–241825	1.8 ± 0.4	1.7 ± 0.4	3.8 ± 0.9	450	2.7	14.34	0.98	1.22		
32	180413.2–242452	1.8 ± 0.4	1.8 ± 0.4	4.0 ± 0.9	452	2.8	15.31	1.35	1.65		
33	180413.8–242619	1.4 ± 0.5	1.3 ± 0.5	5.3 ± 0.9	457	5.4	16.32	1.53	1.98		
34	180413.9–242405	2.6 ± 0.5	2.6 ± 0.5	3.8 ± 1.0	454	1.4	15.59	1.40	1.68		

Table 1. (continued)

Source #	XMMUJ	MOS1 10^{-3} cts s $^{-1}$	MOS2 10^{-3} cts s $^{-1}$	pn 10^{-3} cts s $^{-1}$	SCB	d (arcsec)	V	B - V	V - I	Variability	Comments
[1]	[2]	[3]	[4]	[5]	[6]	[7]	[8]	[9]	[10]	[11]	[12]
35	180414.3–241938	0.8 ± 0.5	1.3 ± 0.5	4.3 ± 1.0	465	3.0	14.39	1.22	1.46		
36	180414.4–242155	7.6 ± 0.7	7.2 ± 0.8	15.9 ± 1.7	470	4.2	13.45	1.20	1.48	N	$P_\mu = 0.00$
37	180414.4–242332	2.2 ± 0.6	1.8 ± 0.6	7.8 ± 1.2	458	7.9	14.61	1.08	1.29		
38	180415.1–242112	1.6 ± 0.4	2.5 ± 0.5	3.3 ± 1.1	480	8.3	16.83	1.49	1.90		
39	180415.8–241457	1.9 ± 0.5	1.3 ± 0.5	3.9 ± 1.0	481	1.8	12.79	0.27	0.42		$P_\mu = 0.76$
40	180416.8–242835	2.4 ± 0.6	1.7 ± 0.5	4.4 ± 1.0	502	2.3	11.56	0.23	0.42		A0, $P_\mu = 0.60$
41	180417.5–242415	2.0 ± 0.5	3.2 ± 0.5	2.4 ± 0.9	504	6.8	14.26	1.22	1.44		
42	180420.2–242250	2.7 ± 0.5	2.8 ± 0.5	6.0 ± 1.1	540	2.3	16.17	1.26	1.76		PMS
43	180420.4–242204	1.2 ± 0.5	1.6 ± 0.6	6.8 ± 1.1	546	3.4	15.43	1.33	1.58		
44	180420.9–242324	2.7 ± 0.5	4.3 ± 0.6	10.8 ± 1.3	556	4.3	16.98	1.41	2.11	N	PMS
45	180421.1–241951	4.2 ± 0.6	4.1 ± 0.6	11.2 ± 1.4	557	2.7	14.71	1.11	1.44	N	
46	180421.8–242039	4.2 ± 0.6	4.7 ± 0.7	13.4 ± 1.6	571	5.9	13.92	0.84	1.06	N	
47	180422.6–242355	5.2 ± 0.7	6.2 ± 0.8		586	4.4	16.81	1.47	1.82	N	
48	180423.6–242951	1.4 ± 0.4	0.8 ± 0.5	2.3 ± 0.8	592	4.3	16.76	1.42	1.79		
49	180424.2–241829	3.2 ± 0.6	1.7 ± 0.5	4.7 ± 0.9	600	2.6	14.19	1.04	1.34		
50	180424.5–242025	2.6 ± 0.5	2.4 ± 0.5	6.7 ± 1.2	607	3.1	16.47	1.45	1.80		
51	180425.0–242747	2.6 ± 0.6	1.3 ± 0.6	7.7 ± 1.3	611	2.0	11.43	0.21	0.41		$P_\mu = 0.70$
52	180425.7–242254	1.9 ± 0.7	3.7 ± 0.9	8.8 ± 1.5	614	6.1	16.32		1.88		
53	180425.8–241750	1.3 ± 0.5	1.3 ± 0.5	2.4 ± 0.9	617	2.7	15.36	1.22	1.50		
54	180425.8–242357	2.8 ± 0.8	2.3 ± 0.7	6.3 ± 1.3	627	8.4	16.69	1.43	1.93		
55	180427.5–242354	1.9 ± 0.6	2.0 ± 0.6	3.6 ± 1.1	641	2.5	13.77	1.09	1.33		
56	180428.6–241855	1.9 ± 0.6	3.9 ± 0.7	6.9 ± 1.3	654	2.3	14.17	0.97	1.19	N	
57	180428.7–241400	1.1 ± 0.6	2.6 ± 0.8	6.6 ± 1.5	656	3.8	11.99	0.52	0.70		$P_\mu = 0.83$
58	180428.7–241444	1.7 ± 0.5	1.2 ± 0.5	6.9 ± 1.4	655	3.0	15.39	0.63	1.52		
59	180429.0–242225	5.1 ± 0.7	6.5 ± 0.8		658	6.5	15.12	1.26	1.57	N	
60	180429.5–242021	3.7 ± 0.6	2.8 ± 0.6	7.3 ± 1.4	665	6.8	16.86	1.54	2.10	N	
61	180431.9–242406	2.6 ± 0.6	2.7 ± 0.6	6.0 ± 1.3	700	7.1	14.59	1.18	1.46		
62	180432.4–242122	2.9 ± 0.6	2.5 ± 0.6	3.1 ± 1.3	698	6.5	16.11	1.41	1.79		
63	180432.9–241844	3.4 ± 0.7	3.1 ± 0.6	9.8 ± 1.6	707	1.5	10.42	0.12	0.19	N	B2.5Vne, $P_\mu = 0.75$
64	180433.6–242706	6.8 ± 1.0	3.5 ± 0.7	7.6 ± 2.0	718	4.2	14.56	1.23	1.57	N	
65	180434.3–241925	2.2 ± 0.6	3.0 ± 0.6	6.3 ± 1.3	725	3.1	12.85	0.87	1.02		$P_\mu = 0.01$
66	180435.5–242729	15.5 ± 1.5	15.7 ± 1.5	50.9 ± 3.7	731	2.0	16.53	1.50	2.03	Y	
67	180437.1–242956	2.2 ± 0.6	1.2 ± 0.6	5.2 ± 1.4	747	2.7	15.02	1.40	1.63		
68	180438.1–242043	1.9 ± 0.6	2.1 ± 0.6	4.0 ± 1.2	761	4.1	15.41	1.40	1.74		
69	180439.1–242409	1.4 ± 0.7	2.3 ± 0.7	6.3 ± 1.4	763	5.7	10.21	1.21	1.27		K0III, $P_\mu = 0.00$
70	180441.8–241855	2.5 ± 0.7	2.6 ± 0.7	6.4 ± 1.4	786	4.1	14.62	1.04	1.24		
71	180441.8–242050	1.4 ± 0.5		2.8 ± 0.9	787	5.9	9.76	0.09	0.18		HD 164947, B2.5 V
72	180450.6–242540	4.3 ± 1.0			879	2.5	11.94	0.39	0.75		LkH α 115 (B4Ve), $P_\mu = 0.79$

Table 2. Same as Table 1 for X-ray sources with two or more counterparts from Sung et al. (2000) inside a radius of 9 arcsec around the position of the X-ray source.

Source #	XMMUJ	MOS1 10^{-3} cts s $^{-1}$	MOS2 10^{-3} cts s $^{-1}$	pn 10^{-3} cts s $^{-1}$	SCB	d (arcsec)	Variability	Comments
[1]	[2]	[3]	[4]	[5]	[6]	[7]	[8]	[9]
73	180338.1–242235	1.8 ± 0.5	1.3 ± 0.5	4.4 ± 0.9	1039/1028	1.7/3.3		^a
74	180340.3–242316	4.9 ± 0.6	5.1 ± 0.8	9.7 ± 1.3	142/146/1019	4.2/5.5/6.8		^b
75	180350.5–242110				240/228/229			240 = LkH α 108 ^c
76	180407.4–242226	7.8 ± 0.8	7.8 ± 0.8		382/380	3.7/4.0	N	
77	180407.7–242311	1.7 ± 0.4	1.4 ± 0.4	1.8 ± 0.7	388/390	2.8/3.2		390 = PMS
78	180414.7–242224	1.5 ± 0.6	3.2 ± 0.6		468/1005	3.2/3.3		1005 = PMS
79	180415.3–241902	0.8 ± 0.4	1.7 ± 0.5	2.6 ± 0.9	478/482	5.0/6.9		482 = PMSc
80	180421.8–242114	1.4 ± 0.8	1.8 ± 0.8	9.7 ± 1.4	573/561/558	5.5/8.0/8.4		
81	180423.0–242116	7.5 ± 0.8	8.3 ± 0.9	14.5 ± 2.1	582/593/587	6.5/8.3/8.7	N	
82	180426.9–242100	2.0 ± 0.5	2.3 ± 0.5	4.5 ± 1.1	631/635	7.1/7.2		
83	180429.1–242147	1.5 ± 0.6	2.0 ± 0.7	4.5 ± 1.5	657/663	5.3/6.1		
84	180429.5–242300	7.7 ± 0.9	7.0 ± 0.9	25.4 ± 2.3	671/659	4.4/7.2	N	
85	180430.7–242634	4.6 ± 0.8	3.7 ± 0.7	7.8 ± 1.4	681/682	2.9/4.1	N	
86	180434.2–242154	1.7 ± 0.5	1.6 ± 0.6	2.8 ± 1.0	723/720/716	4.1/7.0/8.3		
87	180436.0–241959	1.0 ± 0.6	2.3 ± 0.7	3.4 ± 1.0	740/738	3.5/6.8		
88	180439.0–241924	2.0 ± 0.6	2.0 ± 0.6	3.4 ± 1.0	765/773	1.9/8.6		
89	180448.7–242634	10.5 ± 1.4	9.3 ± 1.4		864/862	1.9/6.8	N	862 = PMS

^a SCB 1028 is classified as a PMS star, while SCB 1039 is a PMS candidate (Sung et al. 2000).

^b SCB 142 is a H α emitting star (LkH α 106) while SCB 1019 is a PMS star (Sung et al.).

^c Source # 75 (XMMU J180350.5–242110) lies within the wings of the PSF of 9 Sgr. Therefore no accurate count rates can be provided.

We also reduced a *ROSAT*-PSPC observation of M8 (rp900374n00, integration time 10.4 ksec, JD 2449078.532 – 2449079.569) using the XSELECT software. In this exposure, SCB 253 appears as the third brightest source (after 9 Sgr and HD 164816) with a net count rate of $(6.9 \pm 1.0) \times 10^{-3}$ cts s $^{-1}$ over the entire energy range of the PSPC instrument. Other sources that are detected in this PSPC image are the Hourglass Region, SCB 7, 28, 47, 182, 274, 340, 452/454, 470, # 76, # 95, # 91, # 94 as well as a source which is not seen with *XMM* at RA = 18:04:03.2, DEC = –24:31:08.5 (equinox J2000).

2.2. Spectra

For the spectra, we adopted the redistribution matrices provided by the EPIC instrument teams (versions available in May 2001) and we used the SAS to build the appropriate ancillary response files for each EPIC instrument. The spectra were binned to reach a minimum of 10 counts per channel and the background corrected spectra were analyzed using the XSPEC software (version 11.00). Because of the strong noise in the pn detector below 0.2 keV and the uncertain calibration of the EPIC instruments at low energies, we ignored the binned energy channels below 0.3 keV for the XSPEC fits. Note that for the X-ray sources associated with HD 164816 and SCB 731, we have a total of respectively 300 and 800 net counts for each MOS spectrum. The pn spectra contain about twice as many counts.

We fitted the spectra using either an absorbed one-temperature meka1 thermal plasma model (Mewe et al. 1985,

Kaastra 1992) or an absorbed power law model. The best fitting model parameters are listed in Table 4. In several cases, the fits with a power law with a rather large photon index Γ are slightly better than those with the thermal plasma model. However, these models yield systematically larger N_{H} than the value 0.17×10^{22} cm $^{-2}$ expected from the mean $E(B - V)$ color excess (see Sect. 3 below). More complex models, such as two-temperature meka1 or meka1 + power law models could also improve the χ^2_{ν} . For instance, the spectrum of source # 76 is better fitted ($\chi^2_{\nu} = 0.99$) with a 2-T thermal model with $kT_1 = 0.84$ and $kT_2 = 5.55$ keV. However, we caution that the quality of our spectra is usually not sufficient to distinguish a very hot ($kT \sim$ a few keV) multi-temperature thermal plasma emission from a power law spectrum.

For the 1-T meka1 fits, we are usually left with a number of nearly equivalent solutions corresponding to either intrinsically harder, but less absorbed or more absorbed but intrinsically softer plasma models. Apart from the late O-star HD 164816 (source # 19), all the sources have rather hard spectra with $kT \geq 0.65$ keV.

The spectrum of HD 164816 could be better fitted by adding a second (harder) component to the model, but the properties of this second component are not well constrained by the data. We note that the best fit model yields $N_{\text{H}} = 0.43 \times 10^{22}$ cm $^{-2}$ which is significantly larger than the value of the interstellar column density $0.15^{+0.05}_{-0.04} \times 10^{22}$ cm $^{-2}$ derived by Diplás & Savage (1994) from the interstellar Ly α line. This suggests that part of the fitted absorption could actually arise in circumstellar (i.e. stellar wind) material.

Table 3. X-ray sources detected in NGC 6530 that have no counterpart in the Sung et al. (2000) catalogue and the SIMBAD database within a radius of 9 arcsec.

Source #	XMMUJ	MOS1 10^{-3} cts s $^{-1}$	MOS2 10^{-3} cts s $^{-1}$	pn 10^{-3} cts s $^{-1}$	Variability
[1]	[2]	[3]	[4]	[5]	[6]
90	180252.9–241525	^a	^a	11.4 ± 2.3	
91	180253.3–241955	6.4 ± 1.4		12.7 ± 2.3	N
92	180257.3–242014	3.9 ± 1.1	2.9 ± 1.1	10.4 ± 1.7	
93	180337.5–242116	0.5 ± 0.4	1.1 ± 0.4	2.4 ± 0.7	
94	180339.1–243302	5.1 ± 1.0	6.9 ± 1.1	12.9 ± 1.9	N
95	180351.3–241149	1.8 ± 0.5	1.8 ± 0.6	1.6 ± 0.8	
96	180356.4–242340	1.3 ± 0.4	2.3 ± 0.4	3.9 ± 0.8	
97	180356.5–242018	0.8 ± 0.4	0.4 ± 0.4	1.6 ± 0.8	
98	180357.1–242055	1.8 ± 0.4	1.4 ± 0.5	1.8 ± 0.7	
99	180358.6–242530	6.4 ± 0.7	6.5 ± 0.7	16.0 ± 1.6	?
100	180402.6–242645	2.3 ± 0.5	2.2 ± 0.4		
101	180404.5–241941	0.7 ± 0.3	1.2 ± 0.4	1.2 ± 0.5	
102	180405.0–242511	2.9 ± 0.5	3.4 ± 0.5	9.1 ± 1.1	
103	180405.2–242340	0.8 ± 0.3	1.1 ± 0.4	1.1 ± 0.5	
104	180409.3–241622	1.2 ± 0.4	0.8 ± 0.4	2.6 ± 0.8	
105	180409.3–242017	1.7 ± 0.5	1.4 ± 0.4	2.6 ± 0.8	
106	180412.2–241907	1.5 ± 0.5	1.3 ± 0.5	1.9 ± 0.8	
107	180413.2–241517	1.4 ± 0.5	1.0 ± 0.5	2.2 ± 0.8	
108	180413.9–241722	0.8 ± 0.4	1.3 ± 0.5	3.2 ± 0.9	
109	180419.6–242603	1.1 ± 0.4	1.1 ± 0.4	3.6 ± 1.0	
110	180420.3–241920	0.9 ± 0.4	1.6 ± 0.5	2.6 ± 1.0	
111	180420.4–242810	2.3 ± 0.6	2.4 ± 0.6	5.0 ± 1.2	
112	180424.7–242454	1.9 ± 0.6	1.5 ± 0.5	3.0 ± 0.8	
113	180430.5–242850	1.2 ± 0.5	1.9 ± 0.6	3.4 ± 1.1	
114	180435.0–242334	3.3 ± 0.7	4.2 ± 0.7	10.0 ± 1.6	N
115	180440.3–242643	7.3 ± 1.1	6.9 ± 1.1	19.0 ± 2.4	N
116	180441.9–242248	2.0 ± 0.7	1.9 ± 0.7	7.8 ± 1.4	
117	180441.9–242128	3.8 ± 0.9	1.7 ± 0.7	12.5 ± 1.8	

^a Source #90 (XMMUJ180252.9–241525) lies outside the field of view of the MOS instruments, but is detected as a rather bright source with $(1.14 \pm 0.23) \times 10^{-2}$ cts s $^{-1}$ in the pn image.

Correcting the X-ray flux for the pure interstellar column density only², we infer an ‘intrinsic’ (i.e. at the top of the stellar wind) X-ray luminosity of 5.7×10^{31} erg s $^{-1}$. Adopting a bolometric correction of -3.00 , we infer $\log L_X/L_{bol} = -6.96$ which is in pretty good agreement with the empirical $L_X - L_{bol}$ relation for O-stars proposed by Berghöfer et al. (1997). It is worth pointing out that Howarth et al. (1997) suggested that this star could be an SB2 binary (although no orbital solution exists so far). Provided that the interstellar column alone properly accounts for the low energy absorption, we find that the L_X/L_{bol} ratio yields no evidence for an excess X-ray emission attributable to a wind interaction in a colliding wind binary.

If we assume that $N_H = N_{H,ISM} = 0.17 \times 10^{22}$ cm $^{-2}$ for the other sources, we find that most fits yield kT of a few keV. Note that the spectrum of SCB 731 (Fig. 6) corresponds to the X-ray

² If we correct for the entire (i.e. fitted) column density, we obtain a corrected intrinsic flux that would be about 7 times larger (although a proper wind absorption model, accounting for the ionization of the wind material would be required, see e.g. Waldron et al. 1998).

emission during the flare event, the contribution of the quiescent time intervals to the spectrum being essentially negligible.

3. The nature of the X-ray sources in NGC 6530

We have plotted the X-ray sources with a single optical counterpart in a $(B - V, V)$ colour-magnitude diagram (Fig. 7). For this purpose, we adopted $\langle E(B - V) \rangle = 0.30$, $R_V = A_V/E(B - V) = 3.1$ and $DM = 11.25$ (van den Ancker et al. 1997). Although they found that some highly reddened stars show anomalous extinction, van den Ancker et al. (1997) proposed that the average extinction law of the intercluster material is normal ($R_V = 3.1$).

We caution that there could be a number of foreground (or background) sources that contaminate our sample. Nevertheless, for the sake of simplicity, we have adopted the distance of NGC 6530 for all the sources. In Table 1, we include the membership probability from the proper motion study of van Altena & Jones (1972) whenever this information exists.

Table 4. Best fitting parameters for absorbed thermal plasma *mekal* and absorbed power law models fitted to the EPIC spectra of the brightest X-ray sources in NGC 6530. The observed fluxes quoted in columns [5] and [9] are evaluated over the energy range 0.5 – 5 keV. The quoted uncertainties correspond to formal errors on the spectral fits.

Source #	wabs*mekal				wabs*power			
	N_{H} 10^{22} cm^{-2}	kT keV	χ^2_{ν} (d.o.f.)	flux $\text{erg cm}^{-2} \text{ s}^{-1}$	N_{H} 10^{22} cm^{-2}	Γ	χ^2_{ν} (d.o.f.)	flux $\text{erg cm}^{-2} \text{ s}^{-1}$
[1]	[2]	[3]	[4]	[5]	[6]	[7]	[8]	[9]
11	$0.22^{+0.07}_{-0.05}$	$3.18^{+0.66}_{-0.55}$	0.98 (60)	1.09×10^{-13}	$0.43^{+0.12}_{-0.13}$	$2.49^{+0.30}_{-0.26}$	1.05 (60)	1.07×10^{-13}
19	$0.43^{+0.12}_{-0.13}$	$0.23^{+0.04}_{-0.04}$	1.08 (152)	0.77×10^{-13}				
36	$0.16^{+0.08}_{-0.06}$	$3.05^{+0.65}_{-0.53}$	1.30 (59)	1.09×10^{-13}	$0.49^{+0.11}_{-0.09}$	$2.78^{+0.33}_{-0.29}$	1.07 (59)	1.08×10^{-13}
47	$0.15^{+0.06}_{-0.04}$	$2.95^{+0.66}_{-0.41}$	1.02 (61)	1.17×10^{-13}	$0.43^{+0.12}_{-0.10}$	$2.92^{+0.46}_{-0.37}$	0.82 (61)	1.13×10^{-13}
59	$1.06^{+0.16}_{-0.19}$	$0.70^{+0.27}_{-0.10}$	1.55 (40)	0.65×10^{-13}	$0.42^{+0.14}_{-0.11}$	$2.99^{+0.54}_{-0.40}$	1.01 (40)	0.83×10^{-13}
66	$0.26^{+0.04}_{-0.04}$	$6.64^{+2.27}_{-1.35}$	0.82 (130)	5.24×10^{-13}	$0.34^{+0.07}_{-0.06}$	$1.80^{+0.15}_{-0.15}$	0.78 (130)	5.27×10^{-13}
76	$0.11^{+0.04}_{-0.04}$	$3.54^{+0.91}_{-0.60}$	1.67 (65)	1.05×10^{-13}	$0.32^{+0.08}_{-0.07}$	$2.66^{+0.33}_{-0.29}$	1.35 (65)	1.05×10^{-13}
81	$0.95^{+0.05}_{-0.13}$	$0.65^{+0.17}_{-0.06}$	1.54 (66)	0.89×10^{-13}	$0.41^{+0.12}_{-0.09}$	$3.15^{+0.52}_{-0.40}$	0.95 (66)	1.19×10^{-13}
84	$0.15^{+0.05}_{-0.05}$	$2.92^{+0.74}_{-0.52}$	1.20 (90)	1.13×10^{-13}	$0.35^{+0.09}_{-0.07}$	$2.62^{+0.29}_{-0.25}$	1.21 (90)	1.14×10^{-13}
89	$1.04^{+0.16}_{-0.17}$	$1.01^{+0.11}_{-0.27}$	1.51 (45)	1.26×10^{-13}	$0.42^{+0.13}_{-0.10}$	$2.80^{+0.23}_{-0.36}$	0.75 (45)	1.58×10^{-13}
94	$0.14^{+0.11}_{-0.09}$	$1.78^{+0.64}_{-0.34}$	1.07 (36)	0.67×10^{-13}	$0.72^{+0.91}_{-0.33}$	$4.87^{+2.56}_{-1.72}$	1.24 (36)	0.55×10^{-13}
99	$0.29^{+0.11}_{-0.08}$	$3.59^{+1.07}_{-0.65}$	1.08 (48)	2.22×10^{-13}	$0.43^{+0.13}_{-0.11}$	$2.22^{+0.28}_{-0.25}$	1.19 (48)	2.22×10^{-13}
115	$0.18^{+0.05}_{-0.04}$	$3.49^{+0.79}_{-0.64}$	0.91 (106)	1.71×10^{-13}	$0.40^{+0.10}_{-0.05}$	$2.65^{+0.34}_{-0.29}$	0.79 (106)	1.67×10^{-13}

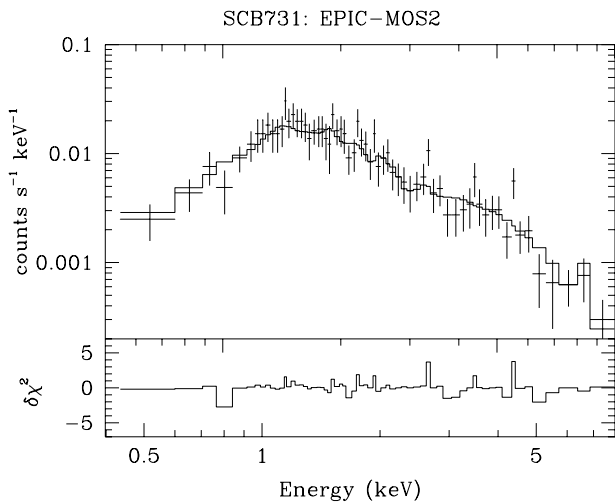


Fig. 6. EPIC-MOS2 spectrum of the X-ray source # 66 associated with SCB 731. The solid line yields the best fitting absorbed *mekal* model.

However, Sung et al. (2000) caution that the proper motion study might be problematic since low membership probabilities were assigned to some early-type stars. In their study, Sung et al. therefore favour purely photometric criteria.

Apart from a group of rather bright ($V \leq 12$) stars that are probably either early-type OB stars, Herbig Ae/Be stars (see below) or foreground objects, we find a group of objects lying to the right of the ZAMS (by about 0.5 in $B - V$). Note that this result is preserved if we adopt the reddening properties suggested by Sung et al. (2000) instead. Five of these objects

display $H\alpha$ emission and are classified as PMS stars (Sung et al. 2000). It seems therefore very likely that this family of X-ray sources corresponds to intermediate- and low-mass PMS objects.

3.1. A population of pre-main sequence stars?

Low-mass PMS stars are classified according to their infrared properties into classes 0, I, II and III (see e.g. Feigelson & Montmerle 1999). Class 0 and I objects are deeply embedded in their nascent molecular cloud and due to their heavy circumstellar extinction, the X-ray emission from these objects is strongly attenuated. These protostars have X-ray luminosities that range from 10^{28} to $10^{30} \text{ erg s}^{-1}$ with occasional flares of order $10^{31} \text{ erg s}^{-1}$ (Carkner et al. 1998) and are best detected in the hard X-rays (e.g. Feigelson & Montmerle 1999). Class II pre-main sequence stars are surrounded by a thick disk. The most distinctive feature of these so-called classical T Tauri stars is their $H\alpha$ emission. Sung et al. (2000) used this criterion to identify 58 PMS stars in NGC 6530 with strong $H\alpha$ emission and 17 PMS candidates with weak $H\alpha$ emission. As the PMS stars evolve, it is thought that their disks dissipate and the PMS stars become Class III objects (or weak-line T Tauri stars) that have weaker or no $H\alpha$ emission. At least in the Taurus-Auriga-Perseus complex, the weak-line T Tauri stars are found to be X-ray brighter than the classical T Tauri stars (Stelzer & Neuhäuser 2001).

The X-ray emission of T Tauri stars is probably due to solarlike magnetic activity or a magnetic interaction with the surrounding protostellar disk. However, the X-ray luminosities

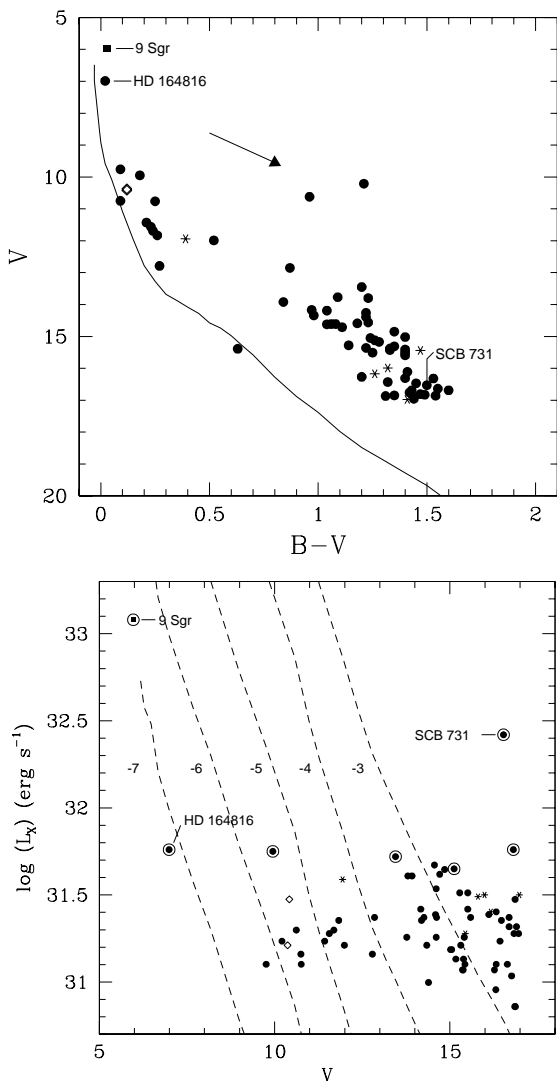


Fig. 7. Top: colour-magnitude diagram of the X-ray sources in the very young open cluster NGC 6530. The reddening vector with $R_V = 3.1$ is indicated and the solid line shows the ZAMS relation taken from Schmidt-Kaler (1982) with a distance modulus $DM = 11.25$ and reddened with $E(B - V) = 0.30$ (see text). Black dots stand for stars from Sung et al. (2000) without $H\alpha$ emission, asterisks stand for pre-main sequence stars or PMS candidates from Sung et al. and the (overlapping) open diamonds indicate two stars classified as Be stars by van den Ancker et al. (1997). Bottom: unabsorbed X-ray luminosity (in the energy range 0.2 – 5.0 keV) as a function of the observed V magnitude. The MOS count rates were converted into luminosities assuming a 2 keV thermal plasma model, a uniform interstellar column density of $N_H = 0.17 \times 10^{22} \text{ cm}^{-2}$ and a distance of 1.8 kpc, except for the sources for which a detailed spectral fit is available. For these sources (symbols surrounded by an open circle) we used the flux from the actual fit. The luminosity of 9 Sgr is taken from Rauw et al. (2002). The dashed lines yield different values of $\log(L_X/L_{bol})$ (indicated by the labels) corresponding to main sequence stars of magnitude V in NGC 6530.

are up to 10^3 times larger than that of the Sun (Neuhäuser 1997). Low-mass PMS stars in the T Tauri stage have multi-temperature thermal X-ray spectra with a soft component in the range $kT_1 \in [0.2, 0.45] \text{ keV}$ and a harder component

with $kT_2 \in [1.3, 2.6] \text{ keV}$. These objects are usually variable X-ray emitters that exhibit flare events with a fast rising curve followed by a slower decay (see e.g. Feigelson & Montmerle 1999 for a review on their high-energy properties).

In the lower panel of Fig. 7, we have plotted the unabsorbed luminosities (in the 0.5 – 5.0 keV band) as a function of V . For the brightest sources, we used the luminosities inferred from the spectral fits in Table 4 and assuming a distance modulus of 11.25. For those sources for which we were not able to perform a spectral fit, we have converted the observed count rates into unabsorbed fluxes assuming a thermal plasma model with $kT = 2 \text{ keV}$, an interstellar column density of $N_H = 5.8 \times 10^{21} \text{ cm}^{-2}$ (Bohlin et al. 1978) and $DM = 11.25$. Note that $kT = 2 \text{ keV}$ is in better agreement with the mean temperature inferred from our spectral fits than the ‘usual’ $kT = 1 \text{ keV}$. Adopting $kT = 1 \text{ keV}$ instead of 2 keV would reduce the luminosities by a factor 0.56 (-0.25 dex).

In summary, among the objects with an intrinsic luminosity exceeding $10^{31} \text{ erg s}^{-1}$ and having a single optical counterpart, there are 57 X-ray sources with an optical counterpart fainter than 12th magnitude and we suggest that most of these objects are good candidates for T Tauri stars. The strong flare that we observe in the light curve of SCB 731 provides further evidence that at least some of these sources are related to PMS stars. The fact that only a few X-ray selected PMS candidates display an $H\alpha$ emission is in agreement with the suggestion that weak-line T Tauri stars are intrinsically X-ray brighter than the classical T Tauri stars (Stelzer & Neuhäuser 2001).

The unabsorbed X-ray luminosities of the brightest sources are found to cluster around a few times $10^{31} \text{ erg s}^{-1}$. Let us emphasize that these values are slightly larger than expected for weak-line T Tauri stars and much larger than those of classical T Tauri stars (Neuhäuser 1997). It seems unlikely that this result is due to uncertainties on the distance of NGC 6530; most of the recent determinations of the cluster distance agree nicely (Sung et al. 2000, van den Ancker et al. 1997). In any case, a sizeable fraction of our sources have L_X/L_{bol} exceeding 10^{-3} . The most likely explanation for these extreme values is that our data only reveal the tip of the X-ray luminosity function of PMS stars in NGC 6530. The cluster could harbour many more PMS stars with X-ray fluxes below our detection threshold ($\sim 4 - 8 \times 10^{30} \text{ erg s}^{-1}$). Assuming $L_X/L_{bol} \sim 10^{-3}$, this X-ray luminosity threshold corresponds to $M_{bol} \sim 4.3$. Most PMS stars less massive than $1.0 M_\odot$ were therefore not detected in our observation.

We have constructed the Hertzsprung-Russell diagram of the X-ray selected stars in NGC 6530 using the T_{eff} versus $V - I$ calibration and the bolometric corrections for main-sequence stars from Kenyon & Hartmann (1995). Figure 8 compares the location of the objects with the pre-main sequence evolutionary tracks of Siess et al. (2000) for $Z = 0.02$ and without overshooting (note that these evolutionary models include neither rotation nor accretion).

We find that the bulk of the X-ray selected PMS stars appear to have masses between 1.0 and $2.0 M_\odot$. A comparison

with the isochrones indicates that most of these objects have ages ranging from 4 to 20 Myr. Only a few more massive objects appear to have ages below 1 Myr. We caution that a comparison of these results with other age determinations of PMS stars in NGC 6530 would be difficult because of the use of different calibrations and to the uncertainties related to the evolutionary calculations (see e.g. the discussion in Siess et al.). However, in Fig. 8, we have also included the PMS stars and candidates selected from their $H\alpha$ emission and which do not appear as X-ray sources in our data. The two samples of PMS stars do not reveal significant age differences, most of the $H\alpha$ selected objects also fall between the 4 and 20 Myr isochrones. This result is quite interesting: at least in NGC 6530 there is no clear evidence for an age difference between weak-line and classical T Tauri stars. This conclusion is in line with the finding of Stelzer & Neuhäuser (2001) that the overall age distribution of weak-line and classical T Tauri stars in the Taurus-Auriga-Perseus region is mixed.

Let us emphasize that there could be a difference in the mass distribution of these two categories of PMS stars. First of all, with the present data sets it is impossible to compare the lower mass limit of the two samples since the $H\alpha$ selection criterion allows to identify fainter (and hence less massive) PMS objects than the X-ray criterion. However, we note that while both categories contain more or less the same number of objects in the $1.0 - 1.5 M_{\odot}$ range, there are many more X-ray selected PMS stars in the $1.5 - 2.0 M_{\odot}$ interval.

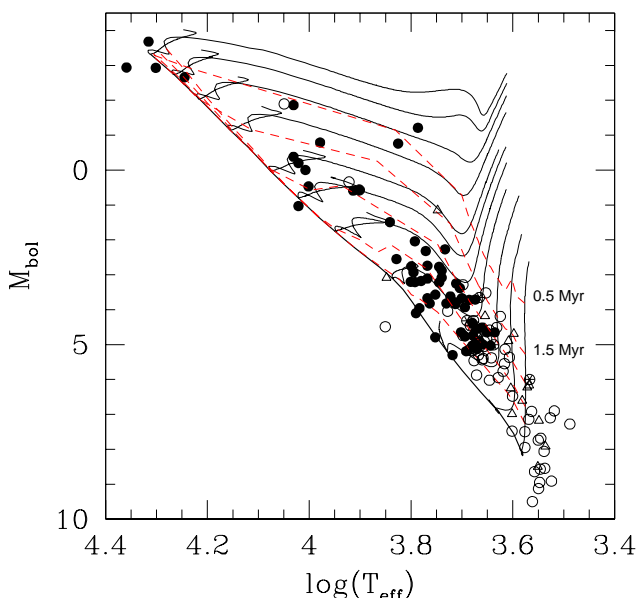


Fig. 8. Hertzsprung-Russell diagram of the X-ray selected stars in NGC 6530. Evolutionary tracks from Siess et al. (2000) for masses of 0.5, 0.7, 1.0, 1.5, 2.0, 2.5, 3.0, 4.0, 5.0, 6.0 and $7.0 M_{\odot}$ are overplotted. Filled symbols indicate X-ray detected objects without $H\alpha$ emission, whereas encircled asterisks stand for PMS stars selected from their $H\alpha$ emission. The open circles and open triangles stand for $H\alpha$ selected PMS and PMSc stars from Sung et al. (2000) respectively. The thick solid line shows the ZAMS, while the dashed lines correspond to isochrones for ages of 0.5, 1.5, 4.0, 10.0 and 20.0 Myr (for clarity only the first two isochrones are labelled).

3.2. Early-type stars

Five Be stars in NGC 6530 were found to exhibit a strong IR excess and were suggested to be Herbig Ae/Be stars by van den Ancker et al. (1997): LkH α 108 (SCB 240), LkH α 112 (SCB 583), LkH α 115 (SCB 879), Walker 29 (SCB 427) and Walker 303. These stars are believed to be intermediate-mass ($\sim 5.5 - 14 M_{\odot}$, van den Ancker et al.) young stellar objects (YSOs). X-ray emission from Herbig Ae/Be YSOs has been reported by Hamaguchi et al. (2001). The objects observed by Hamaguchi et al. (2001) were found to display high temperature thermal emission ($kT \sim 1 - 5$ keV) with luminosities in the range $10^{30} - 10^{32}$ erg s $^{-1}$.

Walker 29 and Walker 303 are not detected in our soft-band X-ray images. LkH α 112 is marginally detected (with a combined likelihood of 9.9), but another star (SCB 581) lies also inside the 9 arcsec radius around the position of the *XMM* source. LkH α 108 lies inside the ‘error box’ of source # 75, together with SCB 228 and 229. The only unambiguous detection of X-ray emission from a Herbig Ae/Be star in our sample concerns LkH α 115 (source # 72), which is detected with an unabsorbed X-ray luminosity of 3.9×10^{31} erg s $^{-1}$. We also note that the X-ray spectrum of source # 11 (SCB 182, B2.5 V) yields a surprisingly high temperature ($kT \sim 3.2$ keV) for a B-star. This suggests that SCB 182 could also be an intermediate-mass YSO, despite the fact that van den Ancker et al. (1997) did not classify it as a Herbig Be star.

High-mass young stellar objects could also emit X-rays. *Chandra* observations of the Orion Nebula Cluster revealed a huge number of X-ray emitting PMS stars over a broad range of masses (Garmire et al. 2000) including the detection of emission from massive stars that are just settling down on the ZAMS. Rho et al. (2001) reported on *ROSAT* and *ASCA* observations of the Trifid Nebula (M 20) which is thought to be in a ‘pre-Orion’ star forming stage. Two massive YSOs as well as one low-mass PMS star were identified as counterparts of *ROSAT* sources. Kohno et al. (2002) obtained a *Chandra* observation of the Monoceros R2 cloud and detected X-ray emission from four massive YSOs which were found to have a mean temperature of $kT \sim 3$ keV and to display flare-like events, much like their low-mass counterparts. This led Kohno et al. (2002) to suggest that the massive YSOs produce X-rays through the same magnetic activity as low-mass PMS stars. This activity would continue until the ZAMS phase and the onset of the stellar wind.

In NGC 6530 it seems rather unlikely to find high-mass YSOs that have not yet reached the ZAMS (at least outside the HG region). In fact, the earliest star in our field of view (apart from 9 Sgr and H 36) is HD 164816 (O9.5 III-IV) which has probably already evolved off the main sequence. Accordingly, van den Ancker et al. (1997) suggested that the formation of stars more massive than $8 M_{\odot}$ has already stopped in NGC 6530. An exception to this rule could be the Hourglass Region which we shall discuss in the next section.

Finally, it is quite remarkable that some of the optically brightest ($V \leq 10.0$) stars in NGC 6530 are not detected in our EPIC data. These include the late-type stars HD 164584, HD 164948 and SCB 444, as well as a number of main-sequence B-type stars (HD 164865, SCB 466, 588, 599, 647, 667 and 708) that have spectral types B1 or slightly later according to van den Ancker et al. (1997). The latter result is somewhat surprising. In fact, *ROSAT* all-sky survey results reported by Berghöfer et al. (1997) suggest that stars of spectral type B1 can have X-ray luminosities of order a few times 10^{31} erg s $^{-1}$ and most of them should therefore be detected in our data. We conclude that most of the early B-type main sequence stars in NGC 6530 may have X-ray luminosities on the lower side of the L_X/L_{bol} relation proposed by Berghöfer et al. (1997).

4. The Hourglass Region

Our EPIC data also reveal X-ray emission from the Hourglass Region in M8. Beside the ionizing star Herschel 36, the HG also harbours the ultra-compact HII region G 5.97–1.17 as well as a number of infrared sources some of which are believed to correspond to embedded massive stars. In fact, Woodward et al. (1990) performed near infrared imaging of the HG, unveiling a Trapezium-like stellar cluster of very young hot stars at the core of the HG. G 5.97–1.17 could be a YSO (probably a late-B star) surrounded by a circumstellar disk that suffers photoevaporation by the radiation from Herschel 36, similar to the so-called proplyds in the Orion Nebula (Stecklum et al. 1998). Herschel 36 is probably a massive YSO that is more evolved than the exciting stars of ultra-compact HII regions. In fact, Stecklum et al. (1995) reported infrared and *HST* H α images that reveal an elongated jet-like structure associated with H 36 oriented roughly perpendicular to the elongated dust structure around the star that could be indicative of a circumstellar disk.

Woodward et al. (1986) proposed a ‘blister’ scenario of the star formation in the HG where the massive star H 36 formed near the edge of the molecular cloud. This picture is also supported by the results of Chakraborty & Anandarao (1997, 1999). These authors studied the kinematics of the HG and found the H II bubble around H 36 to be expanding which suggests that the ionization front is still destroying the surrounding molecular cloud and pressure equilibrium has not yet been reached. In addition, these authors reported high velocity flows to the south of H 36 that indicate a Champagne flow.

The EPIC soft-band image of the HG region (Fig. 9) reveals an extended X-ray emission probably due to the contributions of the young stellar object H 36, the UC HII region and possibly a diffuse emission from a hot bubble created by the wind of Herschel 36. In particular, we find no correlation between the soft X-ray emission and the embedded IR sources discussed by Woodward et al. (1990). While the X-ray emission peaks around the position of H 36, it presents also an enhancement towards the south-east of H 36 (roughly coincident with the southern lobe of the optical HG nebula).

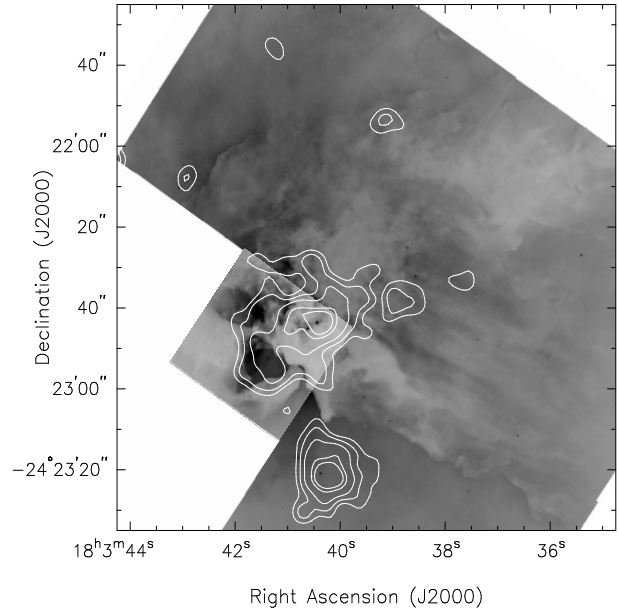


Fig. 9. EPIC X-ray contours superimposed on a *HST* WFPC2 H α image of the HG region in the Lagoon Nebula. The X-ray contours reveal an elongated X-ray source at the location of the O7 V star Herschel 36 and of the UC HII region G 5.97–1.17 as well as an emission lobe extending over the southern part of the optical HG nebula. The EPIC contours were smoothed by convolution with a gaussian of $\sigma = 2$ pixels (1 pixel = 1 arcsec 2) and the contour levels correspond to 0.3, 0.4, 0.55, 0.81 and 1 EPIC (MOS1 + MOS2 + pn) count per arcsec 2 in the 0.5–1.2 keV band. The X-ray source below the HG is associated with SCB 142 and 146 (see Table 2).

Woodward et al. (1986) found that the electron density (4000 cm $^{-3}$) on the eastern side of the ionized cavity is about ten times larger than the electron density on the western side (see their Fig. 15). Therefore, we find that the X-ray emission is enhanced over the higher density part of the HG region.

We have extracted EPIC-MOS spectra of the Hourglass in the energy range 0.2–1.2 keV and fitted them simultaneously with the *ROSAT*-PSPC spectrum extracted from observation rp900374n00. The source counts were extracted over an elliptical area designed to avoid contamination from neighbouring sources. The background-corrected spectra can be fitted ($\chi^2_\nu = 1.25$, 55 d.o.f.) with an absorbed *mekal* model with $N_H = (1.11^{+0.15}_{-0.17}) \times 10^{22}$ cm $^{-2}$, $kT = 0.63^{+0.07}_{-0.05}$ keV. The observed and unabsorbed fluxes in the energy band 0.2–2.0 keV are respectively 1.1×10^{-13} and 1.7×10^{-12} erg cm $^{-2}$ s $^{-1}$. The latter value corresponds to an integrated intrinsic luminosity of 6.6×10^{32} erg s $^{-1}$. Assuming that the X-ray emission from H 36 roughly follows the L_X/L_{bol} relation proposed by Berghöfer et al. (1997), we expect H 36 to contribute 1.5×10^{32} erg s $^{-1}$, i.e. about one fourth of the total X-ray luminosity of the HG region.

Although we cannot completely rule out that the shape of the contours in Fig. 9 might result from the superposition of the PSFs of several faint point sources, it seems very tempting to associate the soft X-ray emission of the HG with a diffuse

emission from a hot plasma around H 36. Diffuse X-ray emission has been observed in a few H II regions only. For instance, Seward & Chlebowski (1982) found an extended diffuse X-ray emission in the Carina Nebula. They attributed the heating of the emitting gas to the interaction of the stellar winds of the rich population of early-type stars with a dense cooler cloud. Wang (1999) reported diffuse X-ray emission arising in blister shaped regions of the 30 Dor complex outlined by loops of H II gas. Such a description could also suit the X-ray emission from the Hourglass Region. On the other hand, recent *Chandra* observations of the massive galactic starburst NGC 3603 revealed an extended diffuse X-ray emission in the immediate surroundings of the cluster core (Moffat et al. 2002). Moffat et al. suggest that the diffuse X-ray emission may arise from multiple merging/colliding hot stellar winds, with a rather low contribution of unresolved PMS stars. Since the HG region is a much less extreme star formation region, a superwind scenario (as in NGC 3603) that would require a large concentration of hot massive stars, is less likely to account for the X-ray emission seen in the HG.

As pointed out above, the density distribution in the vicinity of the Hourglass is believed to be highly non-uniform (Woodward et al. 1986) and a sophisticated numerical model such as the one developed by Comerón (1997) is therefore needed for a detailed comparison. In fact, simulated X-ray maps of a blister model presented by Comerón show that the X-ray emission consists of two components: an extended one from the bubble expanding into the intercloud (low-density) medium and a compact one in the vicinity of the star (i.e. in the high density part still contained in the molecular cloud). The simulations of Comerón (1997) indicate that the intrinsic soft X-ray emission from the compact component should dominate the extended emission component. The observed enhancement of the extended emission over the high density part of the HG is at least in qualitative agreement with this description.

Could the stellar wind of Herschel 36 (O7 V) account for the X-ray luminosity of a wind-blown bubble? The theory of these bubbles has been considered by Castor et al. (1975) and Weaver et al. (1977), with further additions by Mac Low & McCray (1988) and Chu et al. (1995) amongst others. The stellar wind sweeps up a dense shell of material, but within the shell there will be a region of hot shocked gas (see e.g. Strickland & Stevens 1999 for a schematic view of the structure of a wind-blown bubble). Within the framework of this theory, the parameters of the bubble depend upon the wind luminosity of the star, the density of the ambient medium and the age of the bubble (see e.g. Chu et al. 1995).

To derive an order of magnitude estimate, we adopt $T_{\text{eff}} = 39000 \text{ K}$ and $\log(L_{\text{bol}}/L_{\odot}) = 5.31$ for H 36. From these parameters, we expect a mass-loss rate $\dot{M} = 4 \times 10^{-7} M_{\odot} \text{ yr}^{-1}$ and a terminal wind velocity $v_{\infty} = 2300 \text{ km s}^{-1}$ (Howarth & Prinja 1989, Prinja et al. 1990). This yields a kinetic luminosity of the stellar wind ($L_{\text{wind}} = 1/2 \dot{M} v_{\infty}^2$) of $6.7 \times 10^{35} \text{ erg s}^{-1}$. For simplicity, we assume that the ambient density is constant at the higher value

derived by Woodward et al. (1986) with $n_e = 4000 \text{ cm}^{-3}$. Adopting an expansion velocity of the HG of $\sim 10 \text{ km s}^{-1}$ (Chakraborty & Anandarao 1997, 1999) and an angular radius of the cavity in the molecular cloud of about $25''$ (corresponding to 0.2 pc at a distance of 1.78 kpc), we infer a dynamical age of about 20000 yrs.

From these values, we derive the theoretical properties of the bubble surrounding H 36. The central temperature of the bubble should be $\sim 5 \times 10^6 \text{ K}$ (i.e. $kT \sim 0.44 \text{ keV}$), the predicted radius is 0.4 pc and the expected X-ray luminosity amounts to $L_X \sim 10^{35} \text{ erg s}^{-1}$.

We note that the predicted radius is larger than the observed radius. This discrepancy is reminiscent of similar problems reported in the literature when the wind luminosity – age – radius relation from the bubble theory is compared to actual observations (see e.g. Oey 1996, Nazé et al. 2001 and references therein). The most outstanding discrepancy between the model and our observations of the HG region concerns the expected X-ray luminosity which is more than a factor 175 larger than the observed one. Note that mass-loading of the bubble cannot explain the discrepancy since one expects a mass-loaded bubble to be even more X-ray bright (Arthur et al. 1996). Part of this discrepancy may instead be due to our estimate of the kinetic luminosity of the wind of H 36. For instance, Stecklum et al. (1998) noted that the *IUE* spectra of H 36 are similar to those of $\theta^1 \text{ Ori C}$ (HD 37022) and suggested hence that H 36 is close to the ZAMS and has a less developed wind than a typical O7 main sequence star. Assuming a mass-loss rate four times lower and a wind velocity half the values used above, the discrepancy would be reduced to a factor ~ 12 . Note however that Leitherer (1988) derived $\dot{M} = 7.6 \times 10^{-7} M_{\odot} \text{ yr}^{-1}$ and $v_{\infty} = 1650 \text{ km s}^{-1}$ for $\theta^1 \text{ Ori C}$ which yields about the same value of the kinetic luminosity than derived hereabove. Another parameter that might account for some of the discrepancy is the density of the ambient medium. We have adopted a rather large value which should be appropriate for the molecular cloud. However, in the blister scenario, part of the bubble expands into the much lower density intercloud medium and the X-ray luminosity of the bubble around H 36 may be set by the density of the latter.

Although the theoretical values are much higher than the observed X-ray luminosity, we conclude that the kinetic luminosity of the stellar wind of Herschel 36 is most probably sufficient to account for the existence of a wind-blown bubble.

5. Summary and conclusions

Our *XMM-Newton* observation of the Lagoon Nebula (M 8) reveals a cluster of rather faint point-like X-ray sources in addition to the bright O4 star 9 Sgr. We have shown that most of these sources have optical counterparts inside the very young open cluster NGC 6530. We suggest that an important fraction of these sources are associated with low-mass pre-main sequence stars (most probably weak-line T Tauri stars) which were not previously identified as PMS objects because of the lack of strong H α emission. Our results suggest that the

true number of low-mass PMS objects exceeds by more than a factor two the number of objects identified by Sung et al. (2000).

The X-ray selected PMS candidates in NGC 6530 are found to have rather hard spectra with kT of a few keV and their X-ray luminosities (of order of a few times 10^{31} erg s $^{-1}$) are apparently in the higher part of the luminosities of T Tauri stars in the literature. The large number of X-ray sources associated with PMS stars in NGC 6530 may shed some light on the origin of apparently diffuse emission in more distant starburst clusters (e.g. NGC 3603) where source confusion becomes a serious issue.

As to intermediate and high-mass young stellar objects, we found that at least one of the known Herbig Be stars in NGC 6530 exhibits a relatively strong X-ray emission, while most of the early-type main sequence stars of spectral type B1 and later are not detected.

We also report X-ray emission from the massive protostar Herschel 36 as well as probably diffuse emission from the Hourglass Region that might reveal a bubble of hot gas produced by the interaction of the stellar wind of Herschel 36 with the denser part of the molecular cloud. Higher spatial resolution observations of the HG with *Chandra* are needed to confirm the diffuse nature of this emission and to further constrain its morphology.

Acknowledgements. We thank the referee Dr. R.D. Jeffries for valuable comments that helped to significantly improve our manuscript. The Liège team acknowledges support from the Fonds National de la Recherche Scientifique (Belgium) and through the PRODEX XMM-OM and Integral Projects. This research is also supported in part by contracts P4/05 and P5/36 “Pôle d’Attraction Interuniversitaire” (SSTC-Belgium). MCR acknowledges support from ESA-Prodex project No. 13346/98/NL/VJ(ic). This research has made use of the SIMBAD database, operated at CDS, Strasbourg, France and NASA’s Astrophysics Data System Abstract Service.

References

- Arthur, S.J., Henney, W.J., & Dyson, J.E. 1996, *A&A*, 313, 897
 Berghofer, T.W., Schmitt, J.H.M.M., Danner, R., & Cassinelli, J.P. 1997, *A&A*, 322, 167
 Bohlin, R.C., Savage, B.D., & Drake, J.F. 1978, *ApJ*, 224, 132
 Carkner, L., Kozak, J.A., & Feigelson, E.D. 1998, *AJ*, 116, 1933
 Castor, J., McCray, R., & Weaver, R. 1975, *ApJ*, 200, L107
 Chakraborty, A., & Anandarao, B.G. 1997, *AJ*, 114, 1576
 Chakraborty, A., & Anandarao, B.G. 1999, *A&A*, 346, 947
 Chu, Y.-H., Chang, H.-W., Su, Y.-L., & Mac Low, M.-M. 1995, *ApJ*, 450, 157
 Comerón, F. 1997, *A&A*, 326, 1195
 Diplas, A., & Savage, B.D. 1994, *ApJS*, 93, 211
 Feigelson, E.D., & Montmerle, T. 1999, *ARA&A*, 37, 363
 Garmire, G., Feigelson, E.D., Broos, P., Hillenbrand, L.A., Pravdo, S.H., Townsley, L., & Tsuboi, Y. 2000, *ApJ*, 120, 1426
 Hamaguchi, K., Koyama, K., & Yamauchi, S. 2001, *Astronomische Gesellschaft Abstract Series*, 18, Abstract of Contributed Talks and Papers JENAM 2001, MS 07 12
 Hasinger, G., Altieri, B., Arnaud, M., et al. 2001, *A&A*, 365, L45
 Howarth, I.D., & Prinja, R.K. 1989, *ApJS*, 69, 527
 Howarth, I.D., Siebert, K.W., Hussain, G.A.J., & Prinja, R.K. 1997, *MNRAS*, 284, 265
 Jansen, F., Lumb, D., Altieri, B., et al. 2001, *A&A*, 365, L1
 Jeffries, R.D., Thurston, M.R., & Pye, J.P. 1997, *MNRAS*, 287, 350
 Kaastra, J.S. 1992, *An X-ray spectral code for optically thin plasmas*, Internal SRON-Leiden Report
 Kenyon, S.J., & Hartmann, L. 1995, *ApJS*, 101, 117
 Kohno, M., Koyama, K., & Hamaguchi, K. 2002, *ApJ*, 567, 423
 Leitherer, C. 1988, *ApJ*, 326, 356
 Lightfoot, J.F., Deighton, D.W., Furniss, I., Glencross, W.M., Hirst, C.J., Jennings, R.E., & Poulter, G. 1984, *MNRAS*, 208, 197
 Mac Low, M.-M., & McCray, R. 1988, *ApJ*, 324, 776
 Mewe, R., Gronenschild, E.H.B.M., & van den Oord, G.H.J. 1985, *A&AS*, 62, 197
 Moffat, A.F.J., Corcoran, M.F., Stevens, I.R., et al. 2002, *ApJ*, in press
 Nazé, Y., Chu, Y.-H., Points, S.D., Danforth, C.W., Rosado, M., & Chen, C.H.R. 2001, *AJ*, 122, 921
 Neuhäuser, R. 1997, *Science*, 276, 1363
 Oey, M.S. 1996, *ApJ*, 467, 666
 Prinja, R.K., Barlow, M.J., & Howarth, I.D. 1990, *ApJ*, 361, 607
 Rauw, G., Blomme, R., Waldron, W.L., et al. 2002, *A&A*, submitted
 Rho, J., Corcoran, M.F., Chu, Y.-H., & Reach, W.T. 2001, *ApJ*, 562, 446
 Schmidt-Kaler, T. 1982, *Landolt-Bornstein Catalogue VI/2b*
 Seward, F.D., & Chlebowski, T. 1982, *ApJ*, 256, 530
 Siess, L., Dufour, E., & Forestini, M. 2000, *A&A*, 358, 593
 Stecklum, B., Henning, T., Eckart, A., Howell, R.R., & Hoare, M.G. 1995, *A&A*, 445, L153
 Stecklum, B., Henning, T., Feldt, M., Hayward, T.L., Hoare, M.G., Hofner, P., & Richter, S. 1998, *AJ*, 115, 767
 Stelzer, B., & Neuhäuser, R. 2001, *A&A*, 377, 538
 Stockman, Y., Barzin, P., Hansen, H., Tock, J.P., de Chambure, D., & Gondoin, P. 1998, in *Proceedings of the First XMM Workshop on Science with XMM* held at Noordwijk, The Netherlands, ed. M. Dahlem, (http://xmm.vilspa.esa.es/news/ws1/ws1_papers.html)
 Strickland, D.K., Stevens, I.R. 1999, *MNRAS*, 306, 43
 Strüder, L., Briel, U., Dennerl, K., et al. 2001, *A&A*, 365, L18
 Sung, H., Chun, M.-Y., & Bessell, M.S. 2000, *AJ*, 120, 333 (SCB)
 Turner, M.J.L., Abbey, A., Arnaud, M., et al. 2001, *A&A*, 365, L27
 van Altena, W.F., & Jones, B.F. 1972, *A&A*, 20, 425
 van den Ancker, M.E., Thé, P.S., Feinstein, A., Vázquez, R.A., de Winter, D., & Pérez, M.R. 1997, *A&AS*, 123, 63
 Waldron, W.L., Corcoran, M.F., Drake, S.A., & Smale, A.P. 1998, *ApJS*, 118, 217
 Wang, Q.D. 1999, *ApJ*, 510, L139
 Weaver, R., McCray, R., Castor, J., Shapiro, P., & Moore, R. 1977, *ApJ*, 218, 377
 Woodward, C.E., Pipher, J.L., Helfer, H.L., et al. 1986, *AJ*, 91, 870
 Woodward, C.E., Pipher, J.L., Helfer, H.L., & Forrest, W.J. 1990, *ApJ*, 365, 252